Yale University
Department of Computer Science

**Cryo-EM Structure Determination through
Eigenvectors of Sparse Matrices**

Ronald. R. Coifman   Yoel Shkolnisky
Fred J. Sigworth   Amit Singer

Cryo-EM Structure Determination through Eigenvectors of Sparse Matrices

Ronald. R. Coifman*, Yoel Shkolnisky*, Fred J. Sigworth†
and Amit Singer*

Abstract

Recovering the three-dimensional structure of proteins is important for understanding their functionality. We describe a spectral graph algorithm for reconstructing the three-dimensional structure of molecules from their cryo-electron microscopy images taken at random unknown orientations. The key idea of the algorithm is designing a sparse operator defined on the projection images, whose eigenvectors reveal their orientations.

The special geometry of the problem rendered by the Fourier projection-slice theorem is incorporated into the construction of a weighted graph whose vertices are the radial Fourier lines and whose edges are linked with the common line property. The radial lines are associated with points on the sphere and are networked through spider like connections. The graph organizes the radial lines on the sphere in a global manner that reveals the projection directions. This organization is derived from a global computation of a few eigenvectors of the graph's adjacency matrix. Once the directions are obtained, the molecule can be reconstructed using classical tomography methods.

---

*Department of Mathematics, Program in Applied Mathematics, Yale University, 10 Hillhouse Ave. PO Box 208283, New Haven, CT 06520-8283 USA. {coifman-ronald@yale.edu, yoel.shkolnisky@yale.edu, amit.singer@yale.edu}

†Department of Cellular and Molecular Physiology, Yale University School of Medicine, 333 Cedar Street, New Haven, CT 06520 USA. fred.sigworth@yale.edu

The presented algorithm is direct (as opposed to iterative refinement schemes), does not require any prior model for the reconstructed object, and shown to have favorable computational and numerical properties. Moreover, the algorithm does not impose any assumption on the distribution of the projection orientations. Physically, this means that the algorithm successfully reconstructs molecules that have unknown spatial preference.

We also introduce extensions of the algorithm, based on the spectral properties of the operator, which significantly improve its applicability to realistic data sets. These extensions include: particle selection, to filter corrupted projections; center determination to estimate the relative shift of each projection; and, a method to resolve the heterogeneity problem, in cases where a mix of different molecules is being imaged concurrently.

1   Introduction

"Three dimensional electron microscopy" [1] is the name commonly given to methods in which the 3D structures of macromolecular complexes are obtained from sets of images taken by an electron microscope. The most widespread and general of these methods is single-particle reconstruction (SPR). In SPR the 3D structure is determined from images of randomly oriented and positioned identical macromolecular "particles", typically complexes 500 kDa or larger in size. The SPR method has been applied to images of negatively stained specimens, and to images obtained from frozen-hydrated, unstained specimens [2]. In the latter technique, called cryo-electron microscopy (cryo-EM) the sample of macromolecules is rapidly frozen in a thin ($\sim$ 100 nm) layer of vitreous ice, and maintained at liquid nitrogen temperature throughout the imaging process.

SPR from cryo-EM images is of particular interest because it promises to be an entirely general technique. It does not require crystallization or

other special preparation of the complexes to be imaged, and in the future it is likely to reach sufficient resolution (~ 0.4 nm) to allow the polypeptide chain to be traced and residues identified in protein molecules [3]. Even at the present best resolutions of 0.9–0.6 nm, many important features of protein molecules can be determined [4].

Much progress has been made in algorithms that, given a starting 3D structure, are able to refine that structure on the basis of a set of negative-stain or cryo-EM images, which are taken to be projections of the 3D object. Data sets typically range from 10^4 to 10^5 particle images, and refinements require tens to thousands of CPU-hours. As the starting point for the refinement process, however, some sort of ab initio estimate of the 3D structure must be made. Present algorithms are based on the "Angular Reconstitution" method of van Heel [5] in which a coordinate system is established from three projections, and the orientation of the particle giving rise to each image is deduced from common lines among the images.

A serious limitation and an active area of research in SPR image processing is the problem of heterogeneity [6, 7]. Often a set of images is obtained from a mixture of particles of two or more different kinds or different conformations. Because traditional SPR methods assume identical particles, they fail to distinguish the different particle species. Extremely desirable would be the ability to establish two or more ab initio reconstructions from a single set of images.

We propose *Globally Consistent Angular Reconstitution (GCAR)*, a reconstruction algorithm that does not assume any ab initio model and establishes a globally consistent coordinate system from all projections. The special geometry of the problem rendered by the Fourier projection-slice theorem [8] is incorporated by GCAR into a weighted directed graph whose vertices are the radial Fourier lines and whose edges are linked using the common line property. Radial lines are viewed as points on the sphere and are networked through spider-like connections. The graph organizes the radial lines on the

sphere in a global manner and reveals the projection directions. Such an organization is derived from a global computation of the eigenvectors of the sparse graph matrix. This global averaging property makes GCAR robust to both noise and false detections of common lines. The global organization of the common lines also promises to provide a solution to the problems of center determination and heterogeneity. GCAR is extremely fast because it requires only the computation of a few eigenvectors of a sparse matrix.

Once the directions are revealed by the eigenvectors, the reconstruction is performed using the combination of classical tomography methods together with more recent non-uniform FFT techniques [9, 10].

We have successfully applied similar graph-based approaches to reconstruct two-dimensional structures, such as the Shepp-Logan phantom, from noisy one-dimensional projections taken at random directions [11]. Many of the recent and successful algorithms for nonlinear dimensionality reduction of high-dimensional data, such as locally linear embedding (LLE) [12], Hessian LLE [13], Laplacian eigenmap [14] and diffusion maps [15] involve the computation of eigenvectors of data-dependent sparse kernel matrices. However, such algorithms fail to solve the cryo-EM problem, because the reduced coordinate system that each of them obtains does not agree with the projection directions. On the other hand, GCAR finds the desired coordinate system of projection images, because it is tailored to the geometry of the problem through the Fourier projection-slice theorem.

The organization of this report is as follows. In Section 2 we introduce the cryo-electron microscopy problem, as well as the related mathematical background. We introduce the GCAR operator, which reveals the orientations of the projections, and analyze its properties in Section 3. The algorithm for recovering the projection orientations is summarized in Section 4, together with a few technical implementation details. Examples of applying this algorithm to two phantoms are given in Section 5. In Section 6 we present several useful extensions of the algorithm. In particular, we present how to deter-

mine the center of each projection by utilizing the common-line property in Section 6.1, how to solve the heterogeneity problem, where projections of two types of molecules are mixed together, in Section 6.2, and how to exploit the properties of the GCAR graph to filter out "bad" projections in Section 6.3. We conclude in Section 7 with a summary and a description of future work.

2   Problem Setup

2.1   The physical setting

The cryo-EM reconstruction problem is to find the three-dimensional structure of a molecule given samples of its two-dimensional projection images at unknown random directions. The intensity of pixels in a given projection image corresponds to line integrals of the electric potential induced by the molecule along the path of the electrons. The highly intense electron beam destroys the molecule and it is therefore impractical to take projection images of the same molecule at known different directions, as in the case of classical computerized tomography (CT). In other words, a single molecule can be imaged only once. All molecules are assumed to have the exact same structure; they differ only by their spatial orientation. Thus, every image is a projection of the same molecule but at an unknown random orientation.

The locations of the microscope (source) and the camera/film (detectors) are fixed, while different images correspond to different spatial rotations of the molecule. Every image is thus associated with an element of the rotation group SO(3). If the electric potential of the molecule is $\phi(r)$ in some fixed 'laboratory' coordinate system $r = (x, y, z)$, then rotating the molecule by $g \in \mathrm{SO}(3)$ results in the potential $\phi_g(r) = \phi(g^{-1}r)$. The projection image $P_g(x, y)$ is obtained by integrating $\phi_g(r)$ along the z-direction (the source-detector direction)

$$P_g(x, y) = \int_{-\infty}^{\infty} \phi_g(x, y, z) \, dz.$$

6
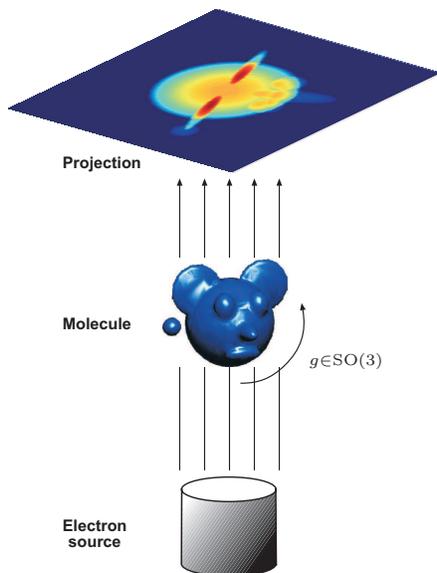
Figure 2.1: Schematic drawing of projection.

The projection operator is also known as the X-ray transform [8]. Figure 2.1 is a schematic illustration of the cryo-EM setting.

The projection image is a digital picture given as an $p \times p$ grid of pixels $P_g = \{P_g(x_i, y_j)\}_{i,j=1}^p \in \mathbb{R}^{p^2}$, where p is determined by the characteristics of the imaging setup.

The cryo-EM problem is stated as follows: find $\phi(x, y, z)$ given a collection of K projections $\{P_{g_k}\}_{k=1}^K$, where g_k are unknown rotations. If the rotations $\{g_k\}_{k=1}^K$ were known then the reconstruction of $\phi(x, y, z)$ could be performed by classical tomography methods. Therefore, the cryo-EM problem is reduced to estimating the rotations $\{g_k\}_{k=1}^K$ given the data set $\{P_{g_k}\}_{k=1}^K$.

For convenience, we adopt the following equivalent point of view. Instead of having the microscope fixed and the molecule oriented randomly in space, we think of the molecule as being fixed, and the microscope being the one that is randomly rotated in space. The orientation of the microscope is described by the beaming direction $\theta \in S^2$ (axis of rotation) and the in-plane rotation

angle $\alpha \in [0, 2\pi)$ of the camera.

2.2   Fourier projection-slice theorem

The two-dimensional Fourier transform of a projection image $P(x, y)$ is given by the double integral

$$\hat{P}(\omega) = \frac{1}{(2\pi)^2} \int_{\theta^\perp} e^{-ir\cdot\omega} P(r) \, dr, \tag{1}$$

where θ is the projection direction, that is, a normal to the image plane. The three-dimensional Fourier transform of the molecule is given by the triple integral

$$\hat{\phi}(\xi) = \frac{1}{(2\pi)^3} \int_{\mathbb{R}^3} e^{-ir\cdot\xi} \phi(r) \, dr. \tag{2}$$

One of the cornerstones of tomography is the Fourier projection-slice theorem stating that the two-dimensional Fourier transform of a projection image is a planar slice $\theta^\perp$ of the three-dimensional Fourier transform of the molecule (see, e.g., [8, p. 11])

$$\hat{P}(\eta) = 2\pi\hat{\phi}(\eta), \quad \eta \in \theta^\perp. \tag{3}$$

Figure 2.2 depicts the geometry induced by the Fourier projection-slice theorem. The sphere represents the 3D Fourier space of the molecule, and the planes are three particular two-dimensional slices of it. As the 2D Fourier transform of a projection image corresponds to a slice of the 3D Fourier space, any two slices share a common line, i.e., the intersection line of the two planes. Figure 2.2 shows three particular slices that happen to share the same common line, marked in dashed black. Note that the effect of rotating the camera (changing α) while fixing the beaming direction θ is an in-plane rotation of the slice without changing its position.

The Fourier transform of each projection image can be considered in polar coordinates as a set of planar radial lines in two-dimensional Fourier space. As a result of the Fourier projection-slice theorem, every planar radial line

8
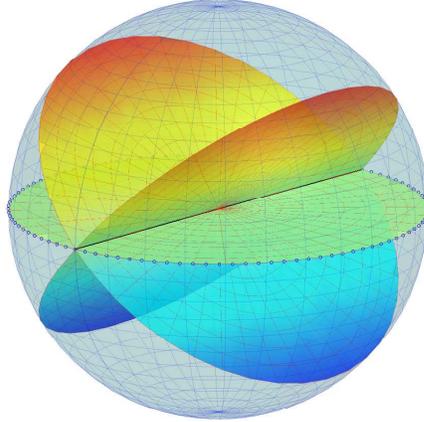
Figure 2.2: Two-dimensional slices of the three-dimensional Fourier space.

is also a radial line in the three-dimensional frequency ball of Fig. 2.2, and there is a one-to-one correspondence between those Fourier radial lines and points on the unit sphere S^2. The radial lines of a single projection image correspond to a great circle (a geodesic circle) on S^2. For example, the radial lines of the green slice in Fig. 2.2 form the equator. Thus, to every projection image P_{g_k} there corresponds a unique great circle $\mathcal{C}_k$ over S^2, and the common line property is restated as follows: any two different geodesic circles over S^2 intersect at exactly two antipodal points.

If the projection directions (the g_k's or the (θ_k, α_k)'s) were known, then the 2D polar Fourier transform of the projection images would have resulted in the values of $\hat{\phi}(\xi)$ on different 3D radial lines, as stated by Eq. 3. Fourier inversion of $\hat{\phi}(\xi)$ in a frequency ball of radius B ($|\xi| < B$, where B is determined by the sampling resolution) would have then reconstructed a band limited approximation of ϕ. However, in the cryo-EM problem the slices are unorganized. Neither their directions θ nor their in-plane rotations α are known.

2.3 Correspondence between Fourier rays and S^2

We next explain the discretization of Fourier space and derive a mapping between the discretized Fourier space and points on the unit sphere S^2. Such a mapping would allow us to proceed by exploiting the simple geometry of S^2.

Let $P_1(x,y), \ldots, P_K(x,y)$ be K projection images. Upon writing the Fourier transform in Eq. 1 in polar coordinates, we obtain

$$\hat{P}_k(\rho, \omega) = \frac{1}{(2\pi)^2} \int \int P_k(x,y) e^{-i(x\rho\cos\omega + y\rho\sin\omega)} \, dx \, dy, \quad k = 1, \ldots, K. \quad (4)$$

For digital implementations we discretize ρ and ω, and compute Eq. 4 using a nonequally-spaced FFT [9]. We denote by L the angular discretization of ω, and sample ρ in n equally-spaced points. That is, we split each transformed projection into L radial lines $\mathbf{\Lambda}_{k,0}, \ldots, \mathbf{\Lambda}_{k,L-1} \in \mathbb{R}^n$, each represented by a set of n equispaced points

$$\mathbf{\Lambda}_{k,l} = \left(\hat{P}_k(B/n, 2\pi l/L), \hat{P}_k(2B/n, 2\pi l/L), \ldots, \hat{P}_k(B, 2\pi l/L) \right) \in \mathbb{R}^n, \quad (5)$$

for $1 \le k \le K$, $0 \le l \le L-1$, where B is the band limit. Note that the DC term ($\rho = 0$ in Eq. 4) is shared by all lines independently of the image and can therefore be ignored.

Let

$$\mathbf{\Lambda}(\boldsymbol{\beta}) = \left(2\pi\hat{\phi}(\boldsymbol{\beta} B/n), 2\pi\hat{\phi}(2\boldsymbol{\beta} B/n), \ldots, 2\pi\hat{\phi}(n\boldsymbol{\beta} B/n) \right) \in \mathbb{R}^n \quad (6)$$

be n samples from a ray through the origin in 3D Fourier space, in a direction given by the unit vector $\boldsymbol{\beta} \in S^2$. This defines a map $\mathbf{\Lambda} : S^2 \to \mathbb{R}^n$ that maps each unit vector in $\mathbb{R}^3$ to n samples of the Fourier ray in that direction. According to the Fourier projection-slice theorem, the radial lines $\mathbf{\Lambda}_{k,l}$ are the evaluations of the function $\mathbf{\Lambda}(\boldsymbol{\beta})$ at the unknown points $\boldsymbol{\beta}_{k,l} \in S^2$. The function $\mathbf{\Lambda}(\boldsymbol{\beta})$ is unknown, because so is $\hat{\phi}$. Our goal is to find the sources

$\boldsymbol{\beta}_{k,l}$ of the overall KL radial lines. The L sources $\{\boldsymbol{\beta}_{k,l}\}_{l=0}^{L-1}$ (k fixed) are equidistant points on the great circle $\mathcal{C}_k \subset S^2$.

3 Orientation Revealing Operator

In this section we introduce the GCAR operator, whose eigenvectors reveal the orientation of each projection. The GCAR operator is a graph with every node representing a ray in Fourier space, and whose edges are determined by the common-line property. The formal construction of this graph is presented in Section 3.1. The normalized adjacency matrix of the graph can be viewed as an averaging operator for functions defined on the nodes of the graph, as explained in Section 3.2. Analyzing the eigenvectors of this operator in Section 3.3 shows that they encode the projection orientations. We conclude by showing in Section 3.4 that the eigenvectors of the GCAR matrix are intimately related to the spherical harmonics.

3.1 GCAR graph

We assume as before that we are given K projection images. Let $\boldsymbol{\Lambda}_{k,l}$, $k = 1, \ldots, K$, $l = 1, \ldots, L$ be KL Fourier rays computed from the K projection images. We think of the radial lines as vertices of a graph, where each radial line $\boldsymbol{\Lambda}_{k,l}$ and its source $\boldsymbol{\beta}_{k,l}$ are identified with the vertex indexed by the pair (k, l). In other words, the set of vertices V of the directed graph $G = (V, E)$ is

$$V = \{(k, l) : 1 \le k \le K, \ 0 \le l \le L - 1\},$$

where the number of vertices is $|V| = KL$. The set $E \subset V \times V$ of directed edges (or arrows)

$$E = \{((k_1, l_1), (k_2, l_2)) : (k_1, l_1) \text{ points to } (k_2, l_2)\}$$

11

will be defined shortly. The graph G is represented using a (sparse) adjacency matrix $\boldsymbol{W}$ of size $KL \times KL$

$$W_{(k_1,l_1),(k_2,l_2)} = \begin{cases} 1 & \text{if} \quad ((k_1,l_1),(k_2,l_2)) \in E \\ 0 & \text{if} \quad ((k_1,l_1),(k_2,l_2)) \notin E. \end{cases}$$

Each row of $\boldsymbol{W}$ corresponds to one radial line in Fourier space $\boldsymbol{\Lambda}_{k,l}$, or alternatively to a point $\boldsymbol{\beta}_{k,l}$ on S^2. The nonzero elements in that row, when viewed on S^2, constitute a spider-like neighborhood, as will be explained shortly.

We now define the set E. Consider a specific vertex (k_1, l_1), that is, the radial line $\boldsymbol{\Lambda}_{k_1,l_1}$. Identify its $2J+1$ neighboring radial lines from its own transformed projection $\hat{P}_{g_{k_1}}$ (indicated in red in the top panel of Fig. 3.1) and set

$$((k_1,l_1),(k_1,l_1+l)) \in E \quad \text{for} \ -J \le l \le J, \tag{7}$$

where addition is modulo L. We link every radial line with J neighboring radial lines in each direction, clockwise and counterclockwise.

We next determine the remaining nonzero entries in row (k_1, l_1) of $\boldsymbol{W}$ by using the common-line property. Whenever we identify $\boldsymbol{\Lambda}_{k_1,l_1} \approx \boldsymbol{\Lambda}_{k_2,l_2}$ as the common line between projection images k_1 and k_2, we add to E the following links

$$((k_1,l_1),(k_2,l_2+l)) \in E \quad \text{for} \ -J \le l \le J. \tag{8}$$

The antipodal rays $\boldsymbol{\Lambda}_{k_1,l_1+L/2}$ and $\boldsymbol{\Lambda}_{k_2,l_2+L/2}$ are common radial lines as well and are linked together in the same manner by setting

$$((k_1,l_1+L/2),(k_2,l_2+L/2+l)) \in E \quad \text{for} \ -J \le l \le J. \tag{9}$$

In general, the adjacency matrix $\boldsymbol{W}$ is nonsymmetric: $((k_1,l_1),(k_2,l_2)) \in E$ (for $k_1 \ne k_2$) reflects the fact that the circle $\mathcal{C}_{k_2}$ containing (k_2,l_2) passes nearby the point (k_1,l_1). However, $\mathcal{C}_{k_1}$ does not necessarily passes nearby
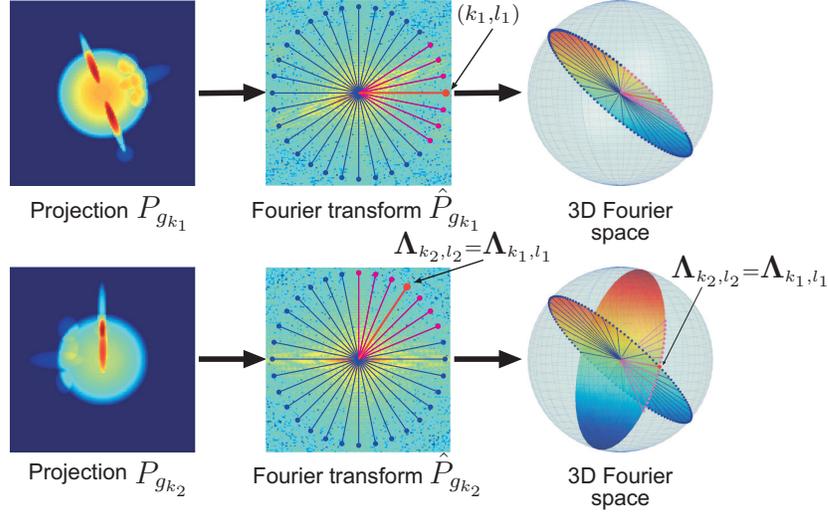
Figure 3.1: Fourier projection-slice theorem.

(k_2, l_2) so $((k_2, l_2), (k_1, l_1)) \notin E$. Symmetry occurs only within the same circle, that is, $((k, l_1), (k, l_2)) \in E \iff ((k, l_2), (k, l_1)) \in E$, which happens whenever $|l_1 - l_2| \leq J$. Although the size of $\boldsymbol{W}$ is $KL \times KL$, by choosing $J \ll L$ we force it to be a sparse matrix. Its number of nonzero entries is only

$$|E| = (2J + 1)KL + 2K(K - 1)(2J + 1). \tag{10}$$

The first summand corresponds to the $2J + 1$ edges in Eq. 7 for each of the KL vertices. The second summand corresponds to edges between different images (Eq. 8). Any two circles intersect at exactly two antipodal points, so there are $2\binom{K}{2} = K(K - 1)$ meeting points. Every meeting point, that is, every common-line $\boldsymbol{\Lambda}_{k_1, l_1} = \boldsymbol{\Lambda}_{k_2, l_2}$ contributes $2J + 1$ nonzero elements in row (k_1, l_1) of $\boldsymbol{W}$, and $2J + 1$ nonzero elements in row (k_2, l_2). In practice, the number of edges in E is smaller than the number in Eq. 10, as explained in Section 4.

If we take row (k_1, l_1) from $\boldsymbol{W}$ and plot the points $\boldsymbol{\beta}_{k,l} \in S^2$ for which

13

(a) One row of $\boldsymbol{W}$ – one spider   (b) Two rows of $\boldsymbol{W}$ – two spiders
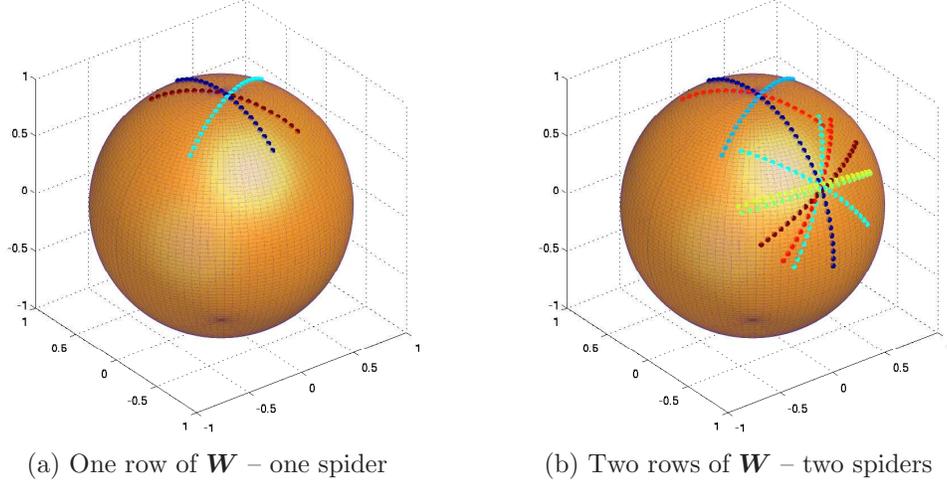
Figure 3.2: Mapping the nonzero entries of $\boldsymbol{W}$ to S^2.

$\boldsymbol{W}_{(k_1,l_1),(k,l)} = 1$, we get a picture that looks like Fig. 3.2a. In light of Fig. 3.2a, we refer to each row of $\boldsymbol{W}$ as the "spider that corresponds to the point (k_1, l_1)". The point $\boldsymbol{\beta}_{k_1,l_1}$ is the head (center) of the spider. Sources $\boldsymbol{\beta}_{k,l}$ that correspond to the same k (come from the same projection image) are marked with the same color. Figure 3.2b shows two spiders on S^2 for a certain randomized choice of circles with $K = 200$, $L = 100$, $J = 10$, from which we can see how different spiders interact. This interaction is essential for the global consistent assignment of coordinates explained below.

Different spiders may have different number of legs, so row sums of $\boldsymbol{W}$ may be different. The outdegree $d_{k,l}$ of the (k, l)'th vertex is the sum of the corresponding row in $\boldsymbol{W}$

$$d_{k,l} = \sum_{(k',l')\in V} W_{(k,l),(k',l')} = |\{(k', l') : ((k, l), (k', l')) \in E\}|. \tag{11}$$

14

3.2 Averaging operator

We normalize the adjacency matrix $\boldsymbol{W}$ to have constant row sums by dividing it by a diagonal matrix $\boldsymbol{D}$ whose diagonal elements equal the outdegrees $d_{k,l}$ of the vertices (or equivalently the row sums of $\boldsymbol{W}$)

$$D_{(k,l),(k,l)} = d_{k,l}, \tag{12}$$

with $d_{k,l}$ given by Eq. 11. This normalization results in the operator

$$\boldsymbol{A} = \boldsymbol{D}^{-1}\boldsymbol{W}. \tag{13}$$

The operator $\boldsymbol{A} : \mathbb{C}^{|V|} \to \mathbb{C}^{|V|}$ takes any discrete complex valued function $\boldsymbol{f} : V \to \mathbb{C}$ (realized as a vector in $\mathbb{C}^{KL}$) and assigns the head of each spider the average of $\boldsymbol{f}$ over the entire spider

$$(\boldsymbol{A}\boldsymbol{f})(k_1, l_1) = \frac{1}{d_{k_1, l_1}} \sum_{((k_1,l_1),(k_2,l_2)) \in E} f(k_2, l_2).$$

We therefore regard A as an averaging operator over $\mathbb{C}^{|V|}$.

The matrix $\boldsymbol{A}$ is row stochastic (the row sums of $\boldsymbol{A}$ all equal 1), and therefore the constant function $\boldsymbol{\psi}_0 = \boldsymbol{1}$ ($\psi_0(v) = 1$, $\forall v \in V$) is an eigenvector with $\lambda_0 = 1$: $\boldsymbol{A}\boldsymbol{\psi}_0 = \boldsymbol{\psi}_0$. The remaining eigenvectors may be complex and come in conjugate pairs, because $\boldsymbol{A}$ is real but not symmetric: $\boldsymbol{A}\boldsymbol{\psi} = \lambda\boldsymbol{\psi} \iff \boldsymbol{A}\bar{\boldsymbol{\psi}} = \bar{\lambda}\bar{\boldsymbol{\psi}}$. As of the spectrum of $\boldsymbol{A}$, $\lambda_0 = 1$ is the largest possible eigenvalue and the remaining eigenvalues reside inside the complex unit disk $|\lambda| < 1$.

3.3 Coordinate eigenvectors

The operator $\boldsymbol{A}$ has many interesting properties. For the cryo-EM problem, the most important property is that the coordinates of the sources $\boldsymbol{\beta}_{k,l}$ are eigenvectors of the averaging operator $\boldsymbol{A}$, sharing the same eigenvalue. Ex-

plicitly, let $x, y, z : \mathbb{R}^3 \to \mathbb{R}$ be the coordinate functions in $\mathbb{R}^3$. Then, the vectors $\boldsymbol{x}, \boldsymbol{y}, \boldsymbol{z} \in \mathbb{R}^{KL}$ defined by

$$\boldsymbol{x} = x(\boldsymbol{\beta}_{k,l}), \quad \boldsymbol{y} = y(\boldsymbol{\beta}_{k,l}), \quad \boldsymbol{z} = z(\boldsymbol{\beta}_{k,l}),$$

$k = 1, \ldots, K$, $l = 1, \ldots, L$ are eigenvectors of A.

This remarkable fact is a consequence of the following observation: the center of mass of every spider is in the direction of the spider's head, because any pair of opposite legs balance each other. For example, the center of mass of a spider whose head is located at the north pole lies just beneath it.

We include the details of the rather technical proof. Suppose $f(x, y, z) = a_1 x + a_2 y + a_3 z = \boldsymbol{a} \cdot \boldsymbol{\beta}$ is a linear function, where $\boldsymbol{a} = (a_1, a_2, a_3)$ and $\boldsymbol{\beta} = (x, y, z) \in S^2$. Consider a spider whose head is at the point $\boldsymbol{\beta}_1 = (x_1, y_1, z_1) \in S^2$, where the value of the function is $f(x_1, y_1, z_1) = \boldsymbol{a} \cdot \boldsymbol{\beta}_1$. Let $\boldsymbol{\beta}_2, \boldsymbol{\beta}_3$ be two unit vectors that complete $\boldsymbol{\beta}_1$ into an orthonormal system of $\mathbb{R}^3$. In other words, the 3×3 matrix $\boldsymbol{U}$ whose columns are $\boldsymbol{\beta}_1, \boldsymbol{\beta}_2, \boldsymbol{\beta}_3$ is orthogonal. We express any point $\boldsymbol{\beta} = (x, y, z)$ on the sphere as a linear combination $\boldsymbol{\beta} = x'\boldsymbol{\beta}_1 + y'\boldsymbol{\beta}_2 + z'\boldsymbol{\beta}_3 = \boldsymbol{U}\boldsymbol{\beta}'$, where $\boldsymbol{\beta}' = (x', y', z')$ is a rotated coordinate system. We apply a change of variable $\boldsymbol{\beta} \to \boldsymbol{\beta}'$ in f to obtain the linear function $f'(x', y', z') = f(x, y, z) = \boldsymbol{a} \cdot \boldsymbol{\beta} = \boldsymbol{a} \cdot \boldsymbol{U}\boldsymbol{\beta}' = \boldsymbol{a}' \cdot \boldsymbol{\beta}'$, where $\boldsymbol{a}' = \boldsymbol{U}^T \boldsymbol{a} = (a'_1, a'_2, a'_3)$. The parameterization of a great circle going through $\boldsymbol{\beta}_1$ is

$$\cos\theta\boldsymbol{\beta}_1 + \sin\theta\cos\varphi_0\boldsymbol{\beta}_2 + \sin\theta\sin\varphi_0\boldsymbol{\beta}_3,$$

where $\theta \in (-\pi, \pi]$ and φ_0 is a fixed parameter that determines the direction of the circle. On that circle, f is a function of the single parameter θ

$$f(\theta) = f'(\cos\theta, \sin\theta\cos\varphi_0, \sin\theta\sin\varphi_0) = \boldsymbol{a}' \cdot (\cos\theta, \sin\theta\cos\varphi_0, \sin\theta\sin\varphi_0).$$

The average $\bar{f}$ of f over the two discrete opposite legs of that circle is

$$\bar{f}(x_1, y_1, z_1) = \frac{1}{2J+1} \sum_{l=-J}^{J} f\left(\frac{2\pi l}{L}\right)$$

$$= \frac{\boldsymbol{a}'}{2J+1} \cdot \sum_{l=-J}^{J} (\cos \frac{2\pi l}{L}, \sin \frac{2\pi l}{L} \cos \varphi_0, \sin \frac{2\pi l}{L} \sin \varphi_0)$$

$$= \left[\frac{1}{2J+1} \sum_{l=-J}^{J} \cos \frac{2\pi l}{L}\right] \boldsymbol{a}' \cdot (1, 0, 0),$$

due to the linearity of the dot product and the fact that $\sin\theta$ is an odd function. From

$$\boldsymbol{a}' \cdot (1, 0, 0) = \boldsymbol{U}^T \boldsymbol{a} \cdot (1, 0, 0) = \boldsymbol{a} \cdot \boldsymbol{U}(1, 0, 0) = \boldsymbol{a} \cdot \boldsymbol{\beta}_1 = f(x_1, y_1, z_1),$$

we conclude that

$$\bar{f}(x_1, y_1, z_1) = \left[\frac{1}{2J+1} \sum_{l=-J}^{J} \cos \frac{2\pi l}{L}\right] f(x_1, y_1, z_1) \tag{14}$$

holds for all (x_1, y_1, z_1) and for any circle going through it. Therefore, linear functions are eigenvectors of the averaging operator $\boldsymbol{A}$ with eigenvalue $\lambda = \frac{1}{2J+1} \sum_{l=-J}^{J} \cos \frac{2\pi l}{L}$. This completes the proof.

3.4 Spherical harmonics

The eigenfunctions of the Laplacian operator on the sphere S^2 are known to be the spherical harmonics Y_l^m [8, p.195](also known as the eigenstates of the angular momentum operator in quantum mechanics)

$$\Delta_{S^2} Y_l^m = -l(l+1)Y_l^m, \quad l = 0, 1, 2, \ldots, \quad m = -l, -l+1, \ldots, l. \tag{15}$$

17

The (non-normalized) spherical harmonics are given in terms of the associated Legendre polynomials of the zenith angle $\theta \in [0, \pi]$ and trigonometric polynomials of the azimuthal angle $\varphi \in [0, 2\pi)$

$$
\begin{aligned}
Y_l^0(\theta, \varphi) &= P_l(\cos \theta), \\
Y_l^m(\theta, \varphi) &= P_l^{|m|}(\cos \theta) \cos m\varphi, \quad 1 \leq m \leq l, \\
Y_l^{-m}(\theta, \varphi) &= P_l^{|m|}(\cos \theta) \sin m\varphi, \quad 1 \leq m \leq l,
\end{aligned}
$$

while the Laplacian is given by

$$
\Delta_{S^2} = \frac{1}{\sin \theta} \frac{\partial}{\partial \theta} \left(\sin \theta \frac{\partial}{\partial \theta} \right) + \frac{1}{\sin^2 \theta} \frac{\partial^2}{\partial \varphi^2}. \tag{16}
$$

The eigenspaces are degenerated so that the eigenvalue $l(l+1)$ has multiplicity $2l + 1$. Alternatively, the l'th eigenspace corresponds to homogeneous polynomials of degree l restricted to S^2. In particular, the first three nontrivial spherical harmonics Y_1^m share the same eigenvalue and are given by the three linear functions

$$
Y_1^1 = x, \quad Y_1^{-1} = y, \quad Y_1^0 = z.
$$

The spherical harmonics Y_l^m are usually derived by separating variables in Eqs. 15–16. However, the fundamental reason for which the spherical harmonics are eigenfunctions of the Laplacian is that the latter commutes with rotations. In fact, the classical Funk-Hecke theorem (see, e.g., [8, p. 195]) asserts that the spherical harmonics are the eigenfunctions of any integral operator $\mathcal{K} : L^2(S^2) \to L^2(S^2)$ that commutes with rotations. Such operators are of the form

$$
(\mathcal{K}f)(\boldsymbol{\beta}) = \int_{S^2} k(\langle \boldsymbol{\beta}, \boldsymbol{\beta}' \rangle) f(\boldsymbol{\beta}') \, dS_{\boldsymbol{\beta}'},
$$

where $k : [-1, 1] \to \mathbb{R}$ is the kernel function that depends only on the angle

between $\boldsymbol{\beta}, \boldsymbol{\beta}' \in S^2$. For such integral operators we have

$$\mathcal{K}Y_l^m = \lambda_l Y_l^m,$$

where the eigenvalues λ_l depend on the specific kernel function $k(\cdot)$ and are given by

$$\lambda_l = 2\pi \int_{-1}^{1} k(t) P_l(t)\, dt.$$

For example, the spherical harmonics are the eigenfunctions of the operator that corresponds to averaging over spherical caps.

The averaging operator $\boldsymbol{A}$ defined in Section 3.2 does not commute with rotations, because every spider has different number of legs that go in different directions. The averaging operator commutes with rotations only in the limit of infinite number of projection images corresponding to a uniform distribution over SO(3) (the Haar measure). Although $\boldsymbol{A}$ does not commute with rotations and the Funk-Hecke theorem does not hold, the coordinate vectors $\boldsymbol{x}, \boldsymbol{y}, \boldsymbol{z} \in \mathbb{R}^{KL}$ span an eigenspace of $\boldsymbol{A}$, due to the center of mass property. Figure 3.3 depicts the first 50 eigenvalues of the operator $\boldsymbol{A}$ constructed using $K = 200$ random points on S^2, $L = 100$ points on each geodesic circle, and $J = 10$ samples on each leg of the spider. This corresponds to using $K = 200$ projection images, $L = 100$ radial Fourier lines for each projection, and using $J = 10$ in Eqs. 7–9. The threefold multiplicity corresponding to the coordinate vectors is clearly seen in Fig. 3.3. Moreover, the observed numerical multiplicities of $1, 3, 5, 7$ and 9 are explained by the spherical harmonics. The remaining eigenvalues seen in Fig. 3.3 correspond to clustering of the circles. By clustering we mean that each of the corresponding eigenvectors takes an almost constant value on one of the circles and practically vanishes on all other circles.
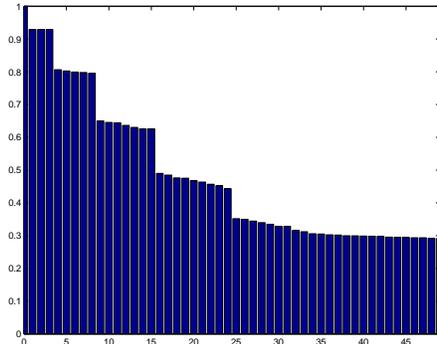
Figure 3.3: Numerical spectra of $\boldsymbol{A}$: $K = 200$, $L = 100$, $J = 10$.

4   Algorithm

The fact that the coordinates $\boldsymbol{x}, \boldsymbol{y}, \boldsymbol{z}$ of the sources $\boldsymbol{\beta}_{k,l}$, $k = 1, \ldots, K$, $l = 1, \ldots, L$, form an eigenspace of $\boldsymbol{A}$ (see Section 3.2) enables to compute them by computing the first three non-trivial eigenvectors $\boldsymbol{\psi}_1, \boldsymbol{\psi_2}, \boldsymbol{\psi}_3$ of the sparse matrix $\boldsymbol{A}$. Taking a sufficiently small J ensures that $\boldsymbol{x}, \boldsymbol{y}, \boldsymbol{z}$ appear immediately after $\boldsymbol{\psi}_0 = \boldsymbol{1}$ in the spectrum of $\boldsymbol{A}$. However, due to the threefold multiplicity of the eigenvalue, the computed eigenvectors may be any linear combination of the coordinate vectors. This linear combination is easily determined (up to an orthogonal transformation) by using the fact that the coordinates must correspond to points on the sphere (i.e., unit length vectors). To this end, we look for a 3×3 matrix $\boldsymbol{M}$ such that

$$\boldsymbol{X} \equiv \begin{pmatrix} - & \boldsymbol{x}^T & - \\ - & \boldsymbol{y}^T & - \\ - & \boldsymbol{z}^T & - \end{pmatrix} = \boldsymbol{M} \begin{pmatrix} - & \boldsymbol{\psi}_1^T & - \\ - & \boldsymbol{\psi}_2^T & - \\ - & \boldsymbol{\psi}_3^T & - \end{pmatrix} \equiv \boldsymbol{M}\boldsymbol{\Psi}. \qquad (17)$$

The diagonal of the $KL \times KL$ matrix $\boldsymbol{X}^T\boldsymbol{X} = \boldsymbol{\Psi}^T\boldsymbol{M}^T\boldsymbol{M}\boldsymbol{\Psi}$ is all ones, because the points are on the unit sphere, that is, $\|\boldsymbol{\beta}_{k,l}\|^2 = x^2(k,l) + y^2(k,l) + z^2(k,l) = 1$. We end up with an overdetermined system of KL linear equa-

20

tions

$$\left(\boldsymbol{\Psi}^T \boldsymbol{M}^T \boldsymbol{M} \boldsymbol{\Psi}\right)_{ii} = 1, \tag{18}$$

for the 9 entries of $\boldsymbol{M}^T \boldsymbol{M}$. The least squares solution for $\boldsymbol{M}^T \boldsymbol{M}$ is then followed by an SVD or a Cholesky decomposition to yield $\boldsymbol{M}$. We can recover $\boldsymbol{M}$ only up to an orthogonal transformation $\boldsymbol{O} \in \mathrm{O}(3)$, because $\boldsymbol{M}^T \boldsymbol{O}^T \boldsymbol{O} \boldsymbol{M} = \boldsymbol{M}^T \boldsymbol{M}$. The reconstruction of the molecule is up to an arbitrary rotation and possibly a reflection (the chirality or handedness cannot be determined).

The locations of the radial lines can be further refined by using the fact that same image radial lines correspond to a great circle on S^2. In particular, such radial lines belong to the same plane (slice). Therefore, we improve the estimation of coordinates by using principal component analysis (PCA) for groups of L radial lines at a time. Furthermore, we equally space those radial lines on the corresponding great circle.

GCAR is summarized in Algorithm 1. Step 3 of finding pairs of common lines can be done efficiently in linear time complexity (instead of comparing a quadratic number of pairs) by approximate nearest neighbors algorithms in a low dimensional feature space. Note that the algorithm assumes that the projection images are centered, for otherwise an arbitrary phase, which alters the step of finding common lines, comes into play. Handling non-centered projections is addressed in Section 6.1.

The eigenvector computation is global and takes into account all the local pieces of information about common lines. Even if some common lines are misidentified, those errors are averaged out in the global eigenvector computation. Thus, GCAR should be regarded as a very efficient way of integrating the local cryo-EM geometry into a global orientation assignment.

The construction of the matrix $\boldsymbol{W}$, as described in Section 3.1, uses all pairs of common lines. That is, for each pair of projection images k_1 and k_2, we find the Fourier lines $\boldsymbol{\Lambda}_{k_1,l_1}$ and $\boldsymbol{\Lambda}_{k_2,l_2}$ such that $\boldsymbol{\Lambda}_{k_2,l_2}$ is closest to $\boldsymbol{\Lambda}_{k_1,l_1}$, and use the pair (k_1, l_1) and (k_2, l_2) to add edges to the set E in Eqs. 8–9.

As can be seen in Fig. 2.2, this corresponds to finding all geodesic circles on S^2 that pass though $\boldsymbol{\beta}_{k_1,l_1}$. Note however, that the coordinates vectors are eigenvectors of $\boldsymbol{A} = \boldsymbol{D}^{-1}\boldsymbol{W}$ even if we use only a few of the geodesic circles that go through $\boldsymbol{\beta}_{k_1,l_1}$. This corresponds to using fewer legs in each spider. Moreover, the resulting matrix $\boldsymbol{W}$ is sparser, and so requires less memory and its eigenvectors can be computed faster. The key advantage of this observation is that we do not need to use all lines determined by the $\binom{K}{2}$ intersection of projection images. We use only pairs of images for which $\boldsymbol{\Lambda}_{k_1,l_1}$ is very close to $\boldsymbol{\Lambda}_{k_2,l_2}$. This results in fewer misidentifications of common-lines, and leads to a more accurate estimation of the orientations. This is demonstrated in Section 5.

Algorithm 1 Outline of GCAR

Require: Projection images $P_k(x,y)$, $k = 1, 2, \ldots, K$
  1: Compute the polar Fourier transform $\hat{P}_k(\rho, \omega)$ (Eq. 4).
  2: Split each $\hat{P}_k(\rho, \omega)$ into L radial lines $\boldsymbol{\Lambda}_{k,l}$ (Eq. 5).
  3: Find common lines $\boldsymbol{\Lambda}_{k_1,l_1} \approx \boldsymbol{\Lambda}_{k_2,l_2}$.
  4: Construct the sparse $KL \times KL$ weight matrix $\boldsymbol{W}$ with $J \ll L$ (following Section 3.1).
  5: Normalize $\boldsymbol{W}$ by its outdegree $\boldsymbol{D}$ and form the averaging operator $\boldsymbol{A} = \boldsymbol{D}^{-1}\boldsymbol{W}$ (Eq. 13).
  6: Compute the first three non-trivial eigenvectors of $\boldsymbol{A}$: $\boldsymbol{A\psi_1} = \lambda\boldsymbol{\psi_1}$, $\boldsymbol{A\psi_2} = \lambda\boldsymbol{\psi_2}$, $\boldsymbol{A\psi_3} = \lambda\boldsymbol{\psi_3}$.
  7: Unmix $\boldsymbol{x}, \boldsymbol{y}, \boldsymbol{z}$ from $\boldsymbol{\psi_1}, \boldsymbol{\psi_2}, \boldsymbol{\psi_3}$.
  8: Refinement: PCA and equally space same image radial lines.

---

5 Numerical Examples

The algorithm was implemented in MATLAB and was tested on two types of phantoms. The first phantom consists of a set of ellipsoids, whose projections can be computed analytically. This phantom is shown in Fig. 5.1a. The second phantom is a $96 \times 96 \times 96$ density map of the E. coli ribosome,

whose projections were computed by approximating line integrals through the volume. The E. coli phantom is pictured in Fig. 5.5a. All tests used $K = 100$ projection images, with $L = 300$ radial Fourier lines per projection, and 100 samples along each Fourier ray. The projections of the analytic phantom were of size 97×97 to avoid half pixel shifts involved in even-size projections. The projections of the E. Coli phantom were of size 96×96 and center estimation was used to compensate for half pixel shifts. The polar Fourier transform was computed as described in [16]. Common-lines between two Fourier-transformed projections were found by computing and comparing correlations between all Fourier lines of the two projections. No knowledge of the orientations or their distribution was used by the algorithm.

All tests were executed on a quad core Xeon 2.33GHz running Linux. Once orientations were determined, the phantom was reconstructed by inter-polating the KL Fourier lines into the three-dimensional pseudo-polar grid by using nearest-neighbor interpolation followed by an inverse 3D pseudo-polar Fourier transform, implemented along the lines of [10, 17].

Figure 5.1a shows a 3D rendering of the analytic phantom, with several of its projections given in Fig. 5.2. The projection orientations for this phantom were randomly sampled from the uniform distribution on S^2. We computed the common line between each pair of projections, that is, the Fourier rays $\mathbf{\Lambda}_{k_1,l_1}$ and $\mathbf{\Lambda}_{k_2,l_2}$, such that $\mathbf{\Lambda}_{k_1,l_1}$ is closest to $\mathbf{\Lambda}_{k_2,l_2}$. Figure 5.3 shows the dissimilarity between $\mathbf{\Lambda}_{k_1,l_1}$ and $\mathbf{\Lambda}_{k_2,l_2}$ for each pair of images k_1 and k_2, sorted from the smallest (most similar) to the largest (most different). Such a plot allows to pick the threshold for filtering the GCAR matrix, as described in Section 4.

Figure 5.4a shows the spectrum of the operator $\mathbf{A}$. Figure 5.4b presents the orientation estimation error. The estimation error for each orientation is defined as the angle (in radians) between the true orientation and the estimated one. Finally, Fig. 5.1b shows the reconstructed phantom. We can see that the reconstructed phantom is related to the original phantom

(a) Original   (b) Reconstructed
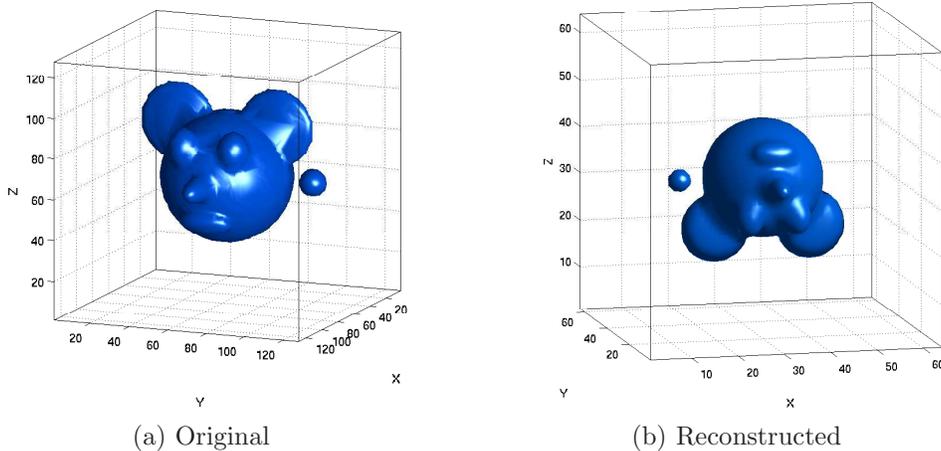
Figure 5.1: Original and reconstructed analytic phantoms.

through an orthogonal transformation, which follows from the multiplicity of the three-dimensional eigenspace.

In Figs. 5.5–5.8 we present the results for the E. coli ribosome density map. Figure 5.5a shows the reference three-dimensional density map of the E. coli ribosome. Several of its projections are given in Fig. 5.6. The orientations in which the projections of this phantom were computed are presented in Fig. 5.7. The spectrum of the corresponding operator A is given in Fig. 5.8. Note that the multiplicities in this spectrum are different than the multiplicities of the spectrum in Fig. 5.4a. The second eigenspace in Fig. 5.8 is of dimension three as the coordinates x, y, and z are always exact eigenvectors, as shown in Section 3.3. However, as opposed to the spectrum in Fig. 5.4a, the next eigenspace is not of dimension five. Due to the distribution of the projection orientations, shown in Fig. 5.7, the resulting GCAR operator does not commute with rotations at all. Hence, the arguments in Section 3.4 do not hold and the spectrum in Fig. 5.8 is not the spectrum of the spherical harmonics. Finally, two views of the reconstructed density map are given in Figs. 5.5b and 5.5c.
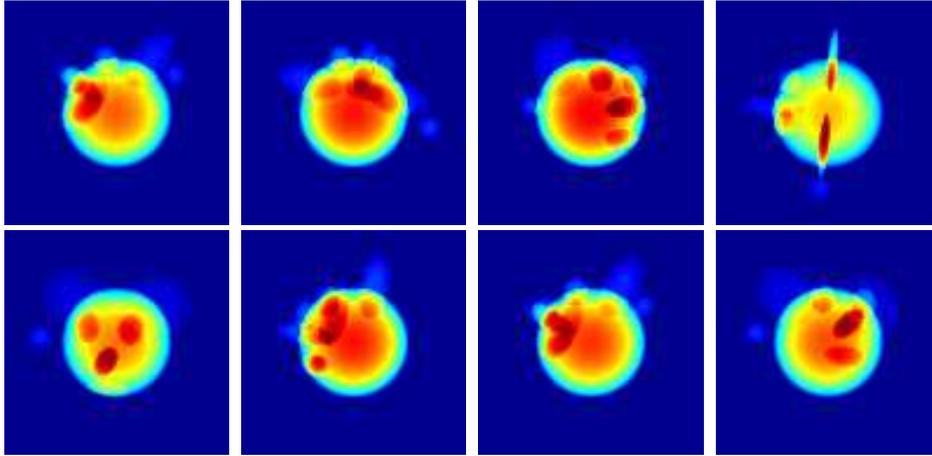
Figure 5.2: Sample of eight projection images of the analytic phantom.
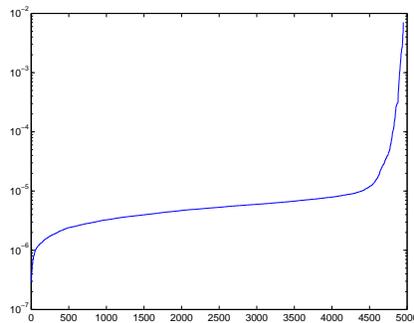
Figure 5.3: Semi-log plot of the dissimilarities between each pair of common lines.
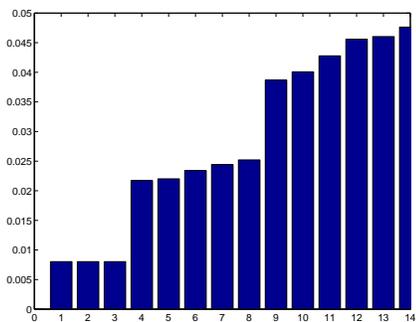
(a) Spectrum of the GCAR operator
$|1 - \lambda_i|$
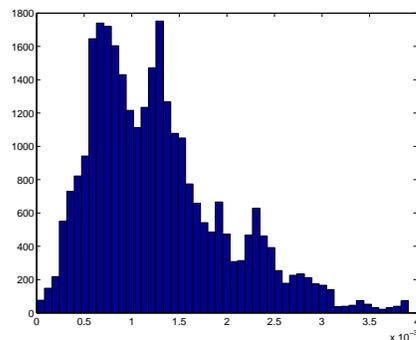
(b) Error histogram

Figure 5.4: Spectrum of the GCAR operator for the analytic phantom and the estimation error histogram.
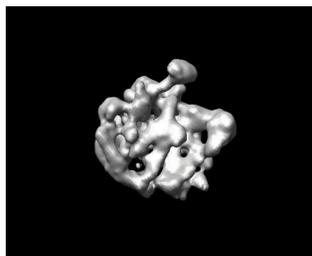
(a) Original
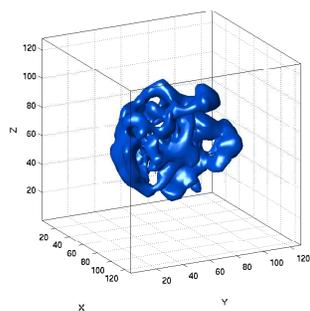
(b) Reconstructed view 1
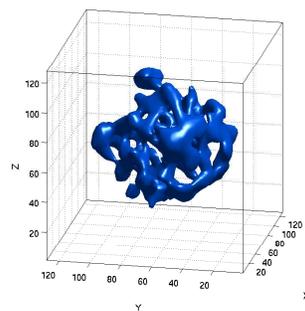
(c) Reconstructed view 2

Figure 5.5: Original and reconstructed E. coli density maps.
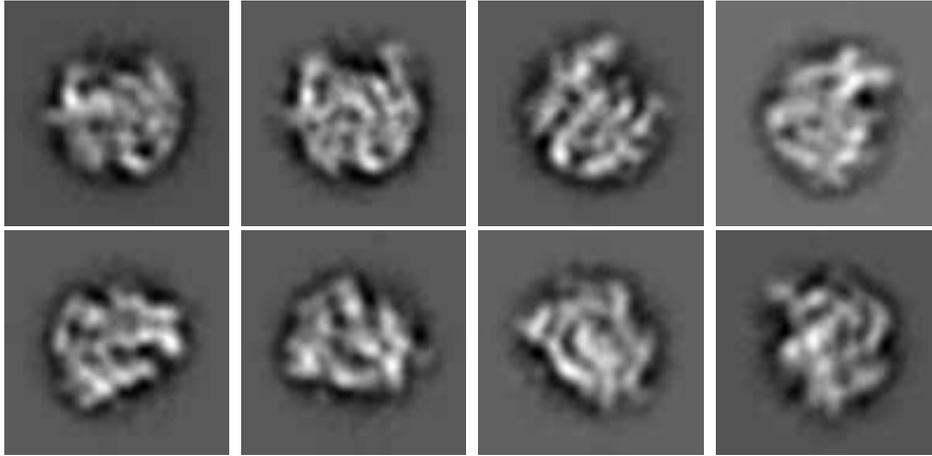
Figure 5.6: Sample of eight projection images of the E. coli ribosome density map.
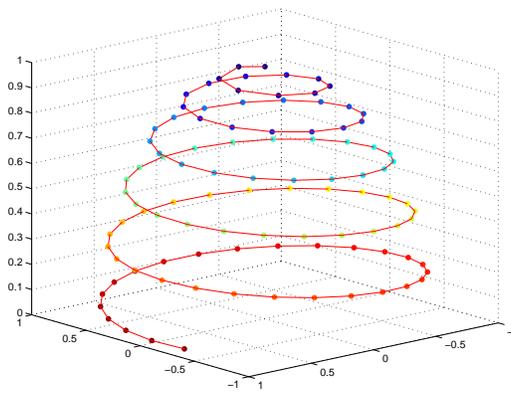
Figure 5.7: Orientations on S^2 used to generate the E. coli projections.
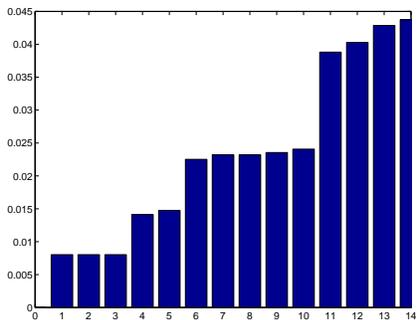
Figure 5.8: Spectrum of the GCAR operator ($|1 - \lambda_i|$) for the E. coli density map.

6 Extensions

6.1 Center determination

The Fourier projection-slice theorem in Section 2.2 requires that for any projection P taken in the direction θ, the center of the imaged object is projected into the center of the projection image P. Such a center, however, has no physical meaning, and any point in the three-dimensional object space can be chosen as the center, by simply putting the origin of the coordinate system at that point. Equation 3 states that this point should be projected into the origin of the coordinate system in all projections.

In practice, each projection image is segmented from a much larger micrograph, containing many projection images, by roughly estimating the bounding box of the imaged molecule's copy. The projections obtained by such a segmentation procedure would not satisfy Eq. 3 simultaneously, because their centers are inconsistent. This means, for example, that defining the center of each projection as its center of mass would lead to inconsistencies.

As a consequence, the input to the cryo-EM problem is a set of projections $Q_{g_1}, \ldots, Q_{g_K}$, where each projection Q_{g_k} contains some unknown shift with respect to its unshifted version P_{g_k} to which the common line property of Eq. 3 can be applied; that is, $Q_{g_k}(x^k, y^k) = P_{g_k}(x^k + \Delta x^k, y^k + \Delta y^k)$, where

Δx^k and Δy^k are the unknown shifts.

The 2D Fourier transform (see also Eq. 4) is given

$$\hat{f}(\omega_x, \omega_y) = \frac{1}{2\pi^2} \iint_{-\infty}^{\infty} f(x, y) e^{-\imath(x\omega_x + y\omega_y)} dx \, dy.$$

By the Fourier shift theorem, if $g(x, y) = f(x + \Delta x, y + \Delta y)$ for some fixed shifts Δx and Δy, then,

$$\hat{g}(\omega_x, \omega_y) = \hat{f}(\omega_x, \omega_y) e^{\imath(\Delta x \omega_x + \Delta y \omega_y)}. \tag{19}$$

Let P_{g_1} and P_{g_2} be two unshifted projections (centered with respect to the center of the underlying three dimensional object). We assume that P_{g_1} uses the coordinate system (x^1, y^1), and P_{g_2} uses the coordinate system (x^2, y^2). Let

$$Q_{g_1}(x^1, y^1) = P_{g_1}(x^1 + \Delta x^1, y^1 + \Delta y^1),$$
$$Q_{g_2}(x^2, y^2) = P_{g_2}(x^2 + \Delta x^2, y^2 + \Delta y^2)$$

be the translated versions of P_{g_1} and P_{g_2}, shifted by $(\Delta x^1, \Delta y^1)$ and $(\Delta x^2, \Delta y^2)$, respectively. The Fourier shift theorem (Eq. 19) implies

$$\hat{Q}_{g_1}(\omega_x^1, \omega_y^1) = \hat{P}_{g_1}(\omega_x^1, \omega_y^1) e^{\imath(\Delta x^1 \omega_x^1 + \Delta y^1 \omega_y^1)},$$
$$\hat{Q}_{g_2}(\omega_x^2, \omega_y^2) = \hat{P}_{g_2}(\omega_x^2, \omega_y^2) e^{\imath(\Delta x^2 \omega_x^2 + \Delta y^2 \omega_y^2)}. \tag{20}$$

Suppose that the common line of the projections $\hat{P}_{g_1}$ and $\hat{P}_{g_2}$ is $(r \cos \theta^1, r \sin \theta^1)$ in $\hat{P}_{g_1}$ and $(r \cos \theta^2, r \sin \theta^2)$ in $\hat{P}_{g_2}$, with θ^1 and θ^2 measured from the w_x-axis in $\hat{P}_{g_1}$ and $\hat{P}_{g_2}$, respectively. Along the common line

$$\hat{P}_{g_1}(r \cos \theta^1, r \sin \theta^1) = \hat{P}_{g_2}(r \cos \theta^2, r \sin \theta^2), \tag{21}$$

and so,

$$
\hat{Q}_{g_1}(r\cos\theta^1, r\sin\theta^1)e^{-ir(\Delta x^1 \cos\theta^1 + \Delta y^1 \sin\theta^1)}
$$
$$
= \hat{Q}_{g_2}(r\cos\theta^2, r\sin\theta^2)e^{-ir(\Delta x^2 \cos\theta^2 + \Delta y^2 \sin\theta^2)},
$$

from which we get

$$
\frac{1}{r}\arg\frac{\hat{Q}_{g_1}(r\cos\theta^1, r\sin\theta^1)}{\hat{Q}_{g_2}(r\cos\theta^2, r\sin\theta^2)} = \mu_{g_1,g_2} \tag{22}
$$

with

$$
\mu_{g_1,g_2} = \Delta x^1 \cos\theta^1 + \Delta y^1 \sin\theta^1 - \Delta x^2 \cos\theta^2 - \Delta y^2 \sin\theta^2. \tag{23}
$$

Given K projection images, there are $2K$ unknowns $(\Delta x^k, \Delta y^k)$ and $\binom{K}{2}$ equations of the form of Eq. 22. Thus we form the $\binom{K}{2} \times 2K$ matrix system of linear equations given by Eq. 22, and solve it using least squares. Note that this linear system is very sparse as each row contains only four nonzero elements. The resulting matrix has a null-space of dimension three, which reflects the fact that arbitrarily moving the origin of the object space $\mathbb{R}^3$ induces another set of consistent translations $(\Delta x^k, \Delta y^k)$ in the projections, which also satisfy Eq. 22. As in the case of constructing the matrix $\boldsymbol{W}$ in Section 3.1, we need not use all $\binom{K}{2}$ equations, but only equations that correspond to highly similar common lines. We can also further filter the system by choosing only equations that correspond to pairs for which the left hand side in Eq. 22 in nearly constant for various values of r. Although in theory the left hand side of Eq. 22 should be constant for all r, this is not the case in practice due to discretization, noise, and measurement errors.

To form the translation estimation equations described above, we need to detect common lines between pairs of projections in the presence of unknown relative shifts. As a result of Eq. 21

$$
|\hat{P}_{g_1}(r\cos\theta^1, r\sin\theta^1)| = |\hat{P}_{g_2}(r\cos\theta^2, r\sin\theta^2)|,
$$

and from Eq. 20 we get

$$|\hat{Q}_{g_1}(r\cos\theta^1, r\sin\theta^1)| = |\hat{Q}_{g_2}(r\cos\theta^2, r\sin\theta^2)|.$$

Hence, to detect common lines between projections that were shifted by some unknown shift, we take the polar Fourier transform of each projection, and find common lines between the magnitude of the Fourier rays.

It may be that two Fourier rays have the same absolute values, although these are not the common line between the two projections. To overcome this problem we find not only the closest pair of rays in $|\hat{Q}_{g_1}|$ and $|\hat{Q}_{g_2}|$, but several such pairs. For each pair we assume it is the common line and estimate the phase factor μ_{g_1,g_2} in Eq. 23 using Eq. 22. Thus we can compute the similarly between the rays $\hat{P}_{g_1}(r\cos\theta^1, r\sin\theta^1)$ and $\hat{P}_{g_2}(r\cos\theta^2, r\sin\theta^2)$ by computing the correlation between $\hat{Q}_{g_1}(r\cos\theta^1, r\sin\theta^1)e^{-ir\mu_{g_1,g_2}}$ and $\hat{Q}_{g_2}(r\cos\theta^2, r\sin\theta^2)$, and choosing the pair θ^1 and θ^2 that brings this correlation to maximum. We then use these θ^1 and θ^2 to form a common line equation of the form of Eq. 22. This results, as explained above, in $\binom{K}{2}$ equations for the $2K$ unknown shifts, which we solve using least-squares.

The performance of the center determination algorithm is demonstrated in Fig. 6.1. We used $K = 100$ projections of the analytic phantom (Fig. 5.1a), each of size 97×97 pixels. An odd size was chosen for the projection images to avoid inherent half-pixel shifts associated with even sampling sizes. Each projection was randomly shifted in the x and y directions by some random shift of up ± 20 pixels in each direction. For each projection we computed $L = 300$ radial Fourier lines, each with $n = 100$ samples in the radial direction. Figure 6.1a shows the 10 smallest singular values of the center estimation system, given by Eq. 22. The null space of dimension three is apparent. Figure 6.1b shows the shifts estimation error. Each bar corresponds to the absolute estimation error (in pixels) in one of the $K = 100$ projections.

31

(a) Smallest singular values of the $\binom{K}{2} \times 2K$ sparse matrix obtained from Eq. 22

(b) Absolute estimation error
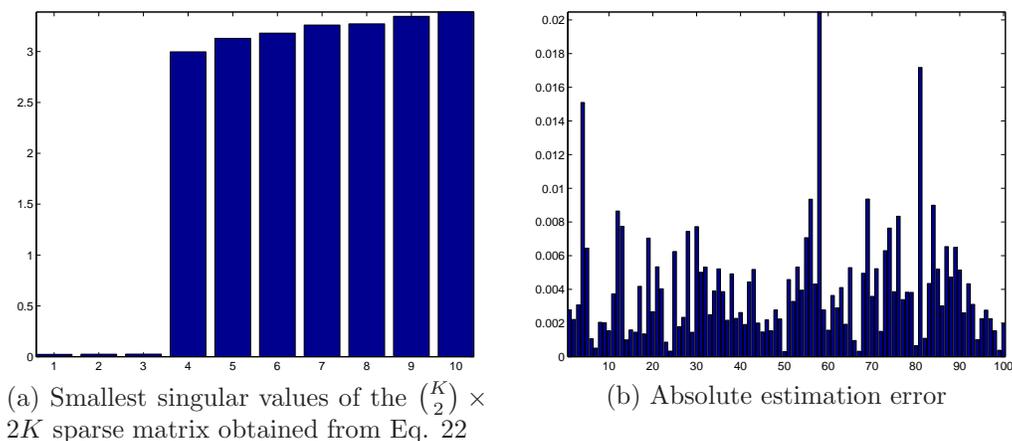
Figure 6.1: Performance of the center estimation algorithm.

(a) Molecule of type 1

(b) Molecule of type 2
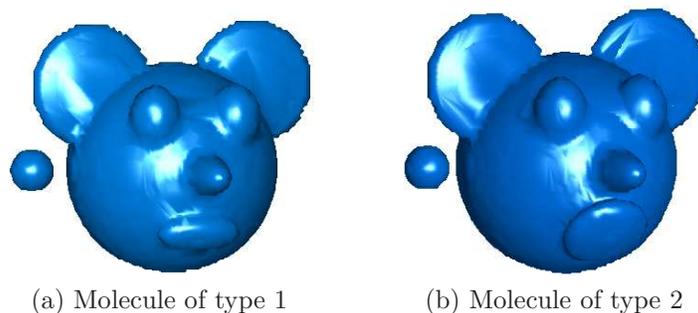
Figure 6.2: Two types of molecules (3D rendering of the analytic phantoms).

6.2 Heterogeneity problem

Suppose our data set contains projections of two different types of molecules. In this section we describe how to use the spectral properties of the operator $\boldsymbol{A}$ defined in Section 3.2 to discriminate between the two different molecules. We will accompany the explanation with an example using two analytic phantoms, depicted in Figs. 6.2a and 6.2b. The example shows only two types of molecules, but essentially the same algorithm can be used to handle more than two types.

Suppose we have a mix of K_1 projections from the first molecule and K_2

projections from the second molecule. Assume for the sake of presentation that the first K_1 projections belong to type 1, and the next K_2 projections belong to type 2. Suppose that we find the common line between any pair of images. For each of the $\binom{K1+K2}{2}$ pairs of images, we obtain the lines $\boldsymbol{\Lambda}_{k_1,l_1}$ and $\boldsymbol{\Lambda}_{k_2,l_2}$, which are supposed to be a common line $\boldsymbol{\Lambda}_{k_1,l_1} = \boldsymbol{\Lambda}_{k_2,l_2}$. We measure the dissimilarity between $\boldsymbol{\Lambda}_{k_1,l_1}$ and $\boldsymbol{\Lambda}_{k_2,l_2}$ and obtain a dissimilarity coefficient dis_{k_1,k_2} corresponding to the pair of projections (k_1, k_2). We expect that on average, the dissimilarity coefficient for two projections that belong to the same type of molecule will be smaller (more similar) than for two projections of different types. Thus, if we sort the dissimilarity coefficients $diss_{k_1,k_2}$, $k_1, k_2 = 1, \ldots, K1 + K2$ from smallest to largest, we expect that the first part of the sorted array will correspond to dissimilarities between projections from the same type of molecule, and the second part of the sorted array, which corresponds to larger dissimilarity coefficients, will correspond to common lines between projections of different types.

To demonstrate this point, we generated a mix that contains $K_1 = 100$ random projections of the molecule of type 1 (Fig. 6.2a) and $K_2 = 100$ random projections of the molecule of type 2 (Fig. 6.2b). The random orientations used for each type of molecule are independent. Each projection is of size 96×96 pixels. To determine common lines, we computed $L = 300$ radial Fourier line in each projection (angular resolution), and used $n = 100$ samples on each Fourier line (radial resolution). We computed the dissimilarity coefficient for each pair of images. The sorted dissimilarity coefficients are shown in Fig. 6.3. As expected, the first part of the sorted list contains small dissimilarity coefficients (roughly half of the list since $K_1 = K_2 = 100$). The second part of the sorted list contains significantly larger values.

If we filter the GCAR matrix $\boldsymbol{W}$, defined in Section 3.1, as descried in Section 4, by retaining only common lines that correspond to the first part of the graph in Fig. 6.3, then the resulting matrix of size $(K_1+K_2)L \times (K_1+K_2)L$ is a block matrix with two non-interacting blocks. Hence, the multiplicities

33
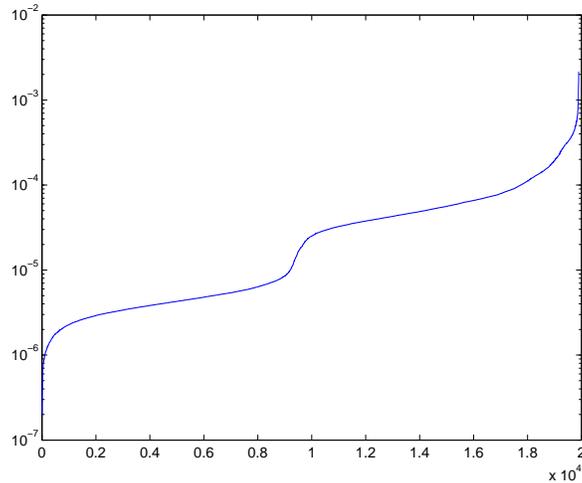
Figure 6.3: Dissimilarity coefficient sorted from smallest to largest.

of the eigenvalues will be doubled compared to the case of a single type of molecule. The spectrum of $\boldsymbol{A}$ for the given heterogeneity example is given in Fig. 6.4.

The first eigenspace (corresponding to eigenvalue 1, or $|1 - \lambda_1| = 0$ in Fig. 6.4) is of dimension two, and the second eigenspace is of dimension six. The first eigenvector, which in the single molecule case is the all-ones vector, now becomes piecewise constant. In fact, by orthogonalizing the first eigenspace of dimension two relative to the all-ones vector, we get a piecewise constant vector $w \in \mathbb{R}^{(K_1+K_2)L}$ such that $w_j > 0$ if Fourier line j belongs to a projection of the first type, and $w_j < 0$ otherwise. The first eigenvector of the mixed GCAR matrix is presented in Fig. 6.5. Figure 6.5 corresponds to the case where the $K_1 + K_2$ projections are randomly shuffled. Only 15000 out of the 60000 entries of the first eigenvector are shown.

We can therefore partition all Fourier lines according to the type of their underlying molecule, and thus classify the projections according to their type. Once partitioned into two classes, the orientations in each class can be determined separately. Figures 6.6a and 6.6b show the sorted dissimilarity coeffi-
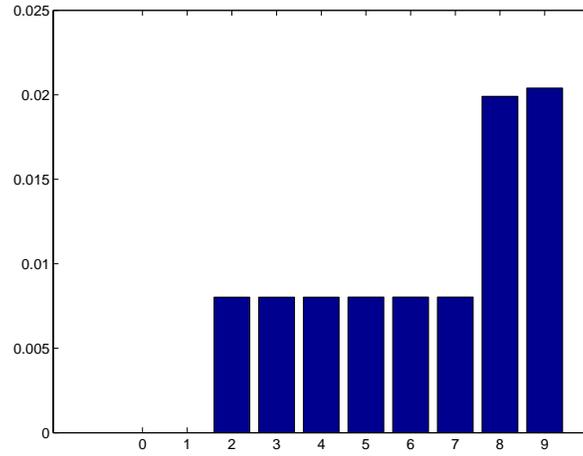
Figure 6.4: Spectrum of the filtered GCAR matrix ($|1 - \lambda_i|$) constructed from a mix of two types of molecules.
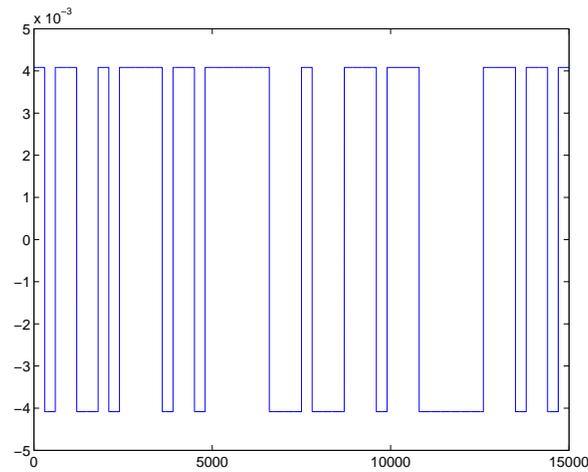

Figure 6.5: First few values of the first eigenvector of the mixed GCAR matrix (after orthogonalizing to the all-ones vector).

(a) Molecule of type 1　　　　　　(b) Molecule of type 2
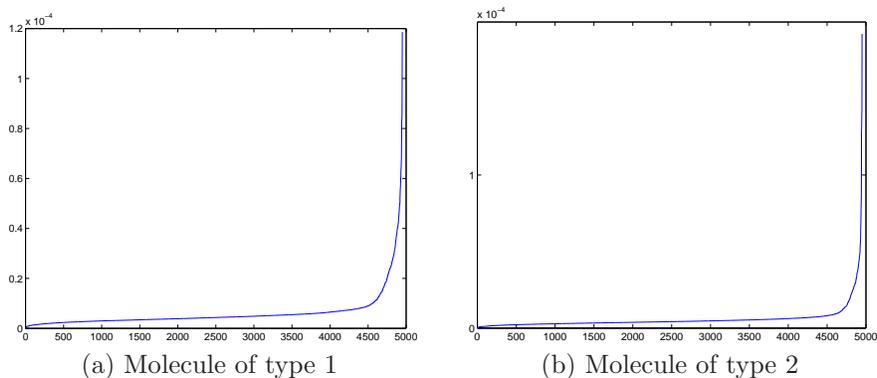
Figure 6.6: Dissimilarity coefficients for each type of molecule.

(a) Molecule of type 1　　　　　　(b) Molecule of type 2
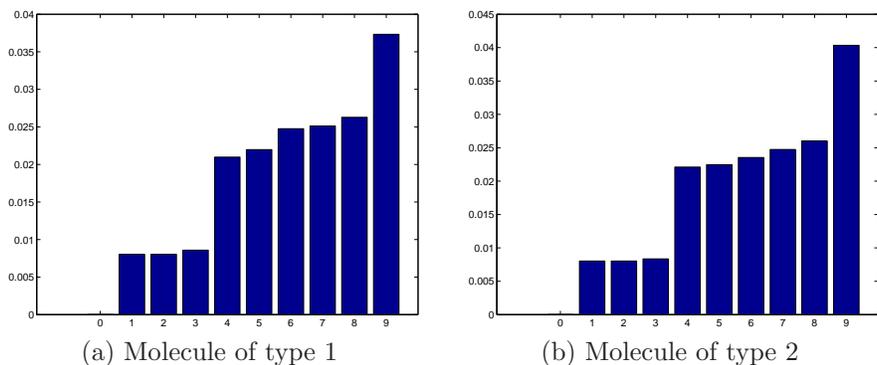
Figure 6.7: Spectrum of the GCAR matrix for each type of molecule.

cient for each type of molecule after classification. The plots in Figs. 6.6a and 6.6b are then used to separately filter the two GCAR matrices corresponding to the individual molecules.

Figures 6.7a and 6.7b show the spectrum of the GCAR matrix of each class. The spectrum for each class is as predicted: the first eigenvalue is 1, and the next subspace is of dimension three. We then estimate the orientations of the projections in each class separately. Histograms of the error estimation are given in Figs. 6.8a and 6.8b.

The advantage of the above procedure is that it uses all the data simul-

36

(a) Molecule of type 1   (b) Molecule of type 2
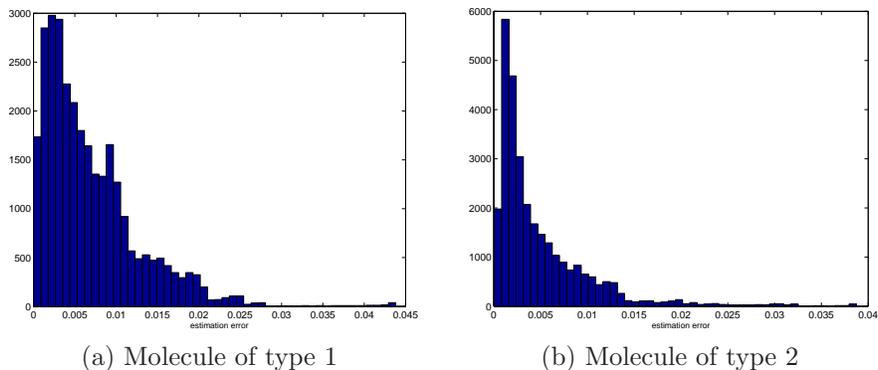
Figure 6.8: Histogram of the orientation estimation error for each type of molecule.

taneously to separate the classes, as opposed to other methods, which try to classify each projection separately.

6.3 Particle selection

The data acquisition process in cryo-electron microscopy generates many projection images which are corrupted by noise, improper segmentation, and overlapping particles, to name but a few. It is desirable to be able to remove such particles from the data set before any reconstruction process takes place. The matrix $\boldsymbol{W}$, defined in Section 3.1, can be used to identify such corrupted projections. Once constructing the matrix $\boldsymbol{W}$, we filter it as described in Section 4. At this point we inspect how many projections intersect a given projection such that the common line between the two projections is highly similar. In theory, in a noiseless setting, any two projections should have a common line. That is, each projection image should have a total of $O(K)$ interactions with other projections. When a projection is corrupted by noise or is otherwise inconsistent with the rest of the projections, there would be only a few such intersections. This would suggest that this projection is inconsistent with the rest of the data set and should be rejected. This
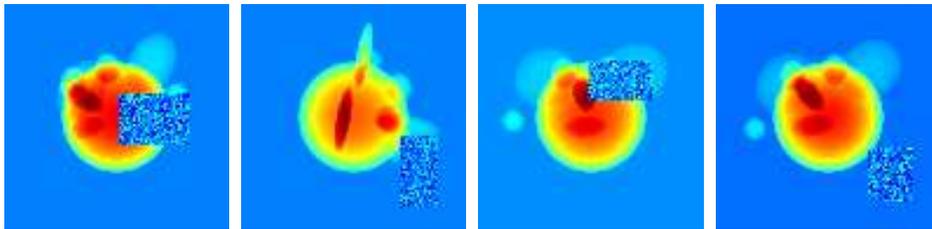
Figure 6.9: Corrupted projections.

again demonstrates the principle that all the data at once should be used to determine which projections are to be used for reconstruction: a projection is "good" if many other projections "say" it is good, by having a common line with it.

To demonstrate this idea we generated $K = 100$ projections of the analytic phantom in Fig. 5.1a, and corrupted 10 projections by a rectangle of Gaussian noise of size up to 10×10 pixels. See Fig. 6.9 for several of these corrupted projections. We then constructed the matrix $\boldsymbol{W}$ as described above, filtered it, and rejected projections that intersect with less than 10 percent of the other projections. Figure 7.1 shows the number of intersections for each projection. The first 20 projections are the corrupted ones. It is clear that by removing projections with a few intersections we retain the "good" projections.

7   Summary and Future Work

In this technical report we introduced a new methodology for the three dimensional cryo-EM structure determination. Our GCAR algorithm incorporates the Fourier-projection slice theorem into a novel construction of a graph, followed by an efficient calculation of a few eigenvectors of the normalized sparse adjacency matrix. The resulting eigenvectors reveal the projection orientations in a globally consistent manner. We demonstrated the success of the method when applied to artificially produced projection images, as well

as its applicability to the image centering and the heterogeneity problems.

The reader must be asking herself if this method would also be successful in practice, when faced with real noisy images, rather than artificially produced clean images. We have good reasons to believe that this would be the case, but at this point of time, we prefer leaving speculation aside. One has to keep in mind that this technical report summarizes a work which is still in progress, and we hope that soon enough we will be able to provide a definite answer.

Not included in this technical report are preliminary results regarding the behavior and success of the GCAR algorithm when the input images are corrupted by white Gaussian noise. Detection of common lines in the presence of noise is much more difficult: out of all detected common lines, only a small percentage are actually true common lines. Although the resulting embedding found by the GCAR algorithm is distorted and cannot be used to reveal the orientations, it can be iteratively improved until convergence to a globally consistent embedding is obtained. In each iteration, we ignore common lines that do not agree with the previously obtained embedding. This iterative procedure, which resembles well known procedures in robust estimation, such as the iterative weighted least squares procedure, cleans up the noisy graph and enables successful reconstructions.

Clearly, denoising of either projection images or radial Fourier lines is a major theme of our future work. We plan to apply both classical and modern denoising methods from image and signal processing. There are two main approaches for denoising the projection images. In the first approach, each projection image will be denoised separately, and the denoised images will be compared to find the common lines. In the second approach, we will try to denoise many images at once, since similar features should appear in different images. A complete discussion of denoising methods and their practical success will be the subject of a future report.
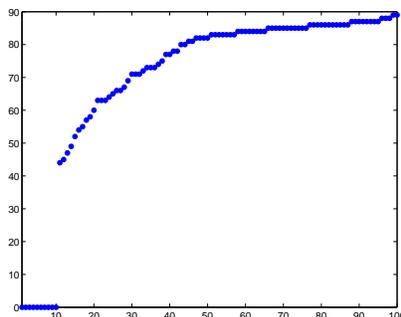
Figure 7.1: Number of intersections of each projection with other projections after filtering the GCAR matrix.

References

[1] J. Frank. *Three-Dimensional Electron Microscopy of Macromolecular Assemblies: Visualization of Biological Molecules in Their Native State.* Oxford, 2006.

[2] L. Wang and F. J. Sigworth. Cryo-em and single particles. *Physiology (Bethesda)*, 21:13–8, 2006. Review. PMID: 16443818 [PubMed - indexed for MEDLINE].

[3] R. Henderson. Realizing the potential of electron cryo-microscopy. *Q Rev Biophys*, 37(1):3–13, 2004. Review. PMID: 17390603 [PubMed - indexed for MEDLINE].

[4] W. Chiu, M. L. Baker, W. Jiang, M. Dougherty, and M .F. Schmid. Electron cryomicroscopy of biological machines at subnanometer resolution. *Structure*, 13(3):363–372, 2005. Review. PMID: 15766537 [PubMed - indexed for MEDLINE].

[5] M. Van Heel. Angular reconstitution: a posteriori assignment of projection directions for 3D reconstruction. *Ultramicroscopy*, 21(2):111–123, 1987. PMID: 12425301 [PubMed - indexed for MEDLINE].

[6] A. E. Leschziner and E. Nogales. Visualizing flexibility at molecular resolution: analysis of heterogeneity in single-particle electron microscopy reconstructions. *Annu Rev Biophys Biomol Struct*, 36:43–62, 2007. Review. PMID: 17201674 [PubMed - indexed for MEDLINE].

[7] S. H. Scheres, H. Gao, M. Valle, G. T. Herman, P. P. Eggermont, J. Frank, and J. M. Carazo. Disentangling conformational states of macromolecules in 3D-em through likelihood optimization. *Nature Methods*, 4(1):27–29, 2007. Epub 2006 Dec 10.

[8] F. Natterer. *The Mathematics of Computerized Tomography*. Classics in Applied Mathematics. SIAM: Society for Industrial and Applied Mathematics, 2001.

[9] A. Dutt and V. Rokhlin. Fast Fourier transforms for nonequispaced data. *SIAM Journal on Scientific Computing*, 14(6):1368–1393, 1993.

[10] A. Averbuch and Y. Shkolnisky. 3D Fourier based discrete radon transform. *Applied and Computational Harmonic Analysis*, 15(1):33–69, 2003.

[11] R. R. Coifman, Y. Shkolnisky, F. J. Sigworth, and A. Singer. Graph laplacian tomography from unknown random projection. *IEEE Transactions on Image Processing*, To appear.

[12] S. T. Roweis and L. K. Saul. Nonlinear dimensionality reduction by locally linear embedding. *Science*, 290(5500):2323–2326, 2000.

[13] D. L. Donoho and C. Grimes. Hessian eigenmaps: Locally linear embedding techniques for high-dimensional data. *Proceedings of the National Academy of Sciences*, 100(10):5591–5596, 2003.

[14] M. Belkin and P. Niyogi. Laplacian eigenmaps for dimensionality reduction and data representation. *Neural Computation*, 15:1373–1396, 2003.

[15] R. R. Coifman, S. Lafon, A. B. Lee, M. Maggioni, B. Nadler, F. Warner, and S. W. Zucker. Geometric diffusions as a tool for harmonic analysis and structure definition of data: Diffusion maps. *Proceedings of the National Academy of Sciences*, 102(21):7426–7431, 2005.

[16] L. Greengard and J.-Y. Lee. Accelerating the nonuniform fast Fourier transform. *SIAM Review*, 46(3):443–454, 2004.

[17] A. Averbuch, R. R. Coifman, D. L. Donoho, M. Israeli, and Y. Shkolnisky. A framework for discrete integral transformations I – the pseudopolar Fourier transform. *SIAM Journal on Scientific Computing*, To appear.